



HAL
open science

Thin Films of SiP Lamellar Alloys: A First Step toward 2D SiP

S. Geiskopf, A. Valdenaire, Mathieu Stoffel, Xavier Devaux, Erwan André, C. Carteret, A. Bouché, M. Vergnat, Hervé Rinnert

► **To cite this version:**

S. Geiskopf, A. Valdenaire, Mathieu Stoffel, Xavier Devaux, Erwan André, et al.. Thin Films of SiP Lamellar Alloys: A First Step toward 2D SiP. *Journal of Physical Chemistry C*, 2021, 10.1021/acs.jpcc.0c11165 . hal-03134056

HAL Id: hal-03134056

<https://hal.science/hal-03134056>

Submitted on 8 Feb 2021

HAL is a multi-disciplinary open access archive for the deposit and dissemination of scientific research documents, whether they are published or not. The documents may come from teaching and research institutions in France or abroad, or from public or private research centers.

L'archive ouverte pluridisciplinaire **HAL**, est destinée au dépôt et à la diffusion de documents scientifiques de niveau recherche, publiés ou non, émanant des établissements d'enseignement et de recherche français ou étrangers, des laboratoires publics ou privés.

Thin Films of SiP Lamellar Alloys: a First Step Towards 2D SiP

S. Geiskopf¹, A. Valdenaire¹, M. Stoffel^{1,*}, X. Devaux¹, E. André², C. Carteret², A. Bouché¹,
M. Vergnat¹, H. Rinnert¹

¹ *Université de Lorraine, CNRS, IJL, F-54000 Nancy, France*

² *Université de Lorraine, CNRS, LCPME, F-54000 Nancy, France*

Abstract

We investigate the structural and vibrational properties of Si:P thin films obtained by co-evaporation of Si and P in ultra-high vacuum at room temperature followed by rapid thermal annealing. The thermal crystallization of the films was followed by Raman spectroscopy. Annealing at temperatures larger than 950 °C leads to the formation of crystalline phases. Density functional theory calculations of the vibrational modes allow us to identify orthorhombic SiP. Electron energy loss spectroscopy combined with energy dispersive spectroscopy give evidence of a plasmon signature of the SiP phase. The distribution of the crystalline phases in the film was imaged by energy filtered transmission electron microscopy. Both Si and SiP areas having sizes of a few microns are found to coexist in the films. High-resolution scanning transmission imaging provides a clear evidence of the lamellar structure while spatially resolved electron energy loss spectroscopy allows us to obtain a chemical mapping for both Si and P atoms, which agrees quite well with the orthorhombic structure of SiP. Our results represent an important first step on the way to obtain 2D SiP, a promising new material for which a direct bandgap has been predicted.

Introduction

Group III-V and group II-VI semiconductor alloys have been extensively studied so far. In contrast, group IV-V alloys have attracted much less attention. Their synthesis and structural properties have been investigated in the late sixties^{1,2} but since then, these compounds have received only little attention. Very recently, however, bulk crystals made of group IV-V materials such as GeP, GeAs, SiAs and SiP were fabricated by using either high pressure melt growth, chemical vapor transport³ or seeded flux growth⁴. They exhibit a monoclinic structure except SiP which crystallizes in an orthorhombic structure. Most importantly, these compounds have a lamellar structure in which strongly two dimensional (2D) covalent layers are stacked onto each other through weaker van der Waals bonds. This property might be of interest for the development of novel 2D semiconductors based on group IV-V materials. For future applications in the field of electronics and optoelectronics, 2D semiconductors exhibiting a direct bandgap, high charge carrier mobilities as well as a good chemical and thermal stability are urgently needed. During the last years, there has been a growing interest in 2D materials based either on group V⁵, V-V⁶ or on group IV-V elements. In particular, orthorhombic 2D SiP has emerged as a potential candidate.

A large number of theoretical papers have addressed the properties of 2D Si_xP_y alloys. It was found that 2D-SiP has one of the lowest formation energy among several other group IV-V 2D materials^{7,8}. The synthesis of 2D SiP by mechanical exfoliation of the bulk material appears thus to be feasible. By using molecular dynamics calculations, Zhang *et al.*⁹ showed that 2D SiP is dynamically and thermodynamically stable even at 900 K. Moreover, it was found that the electronic/optical properties of 2D Si_xP_y alloys¹⁰ can be tuned either by varying the thickness^{8,11}, the stacking¹¹ or by application of an in-plane strain^{8,12,13,14}. Interestingly, a transition from an indirect to a direct bandgap has been predicted when SiP is thinned down to a monolayer^{8,9}. The calculated bandgap (2.59 eV) appears very promising for the development

of 2D blue light emitting diodes. Ma *et al.*¹⁵ and Mortazavi *et al.*¹⁶ further emphasize the potential interest of 2D SiP for photocatalytic water splitting as well as a large absorption coefficient in the near UV and the visible⁸. By combining first principles calculations and semi-classical Boltzmann transport theory, Jiang *et al.*¹⁷ investigate the thermoelectric properties of both GeP and SiP. Highly isotropic Seebeck coefficients as well as rather high ZT values were obtained, which appears promising for future thermoelectric applications. Finally, Zhou *et al.*¹⁸ studied the electronic properties of complex van der Waals heterostructures containing 2D SiP layers and showed that they can be modulated by the application of either out-of-plane or in-plane strain.

In contrast to the large number of recent theoretical investigations, experimental studies on either bulk SiP crystals or Si:P thin films are rather scarce. Barreteau *et al.*³ used high pressure melt growth and chemical vapor transport to produce bulk, orthorhombic SiP crystals. Resistivity measurements indicate a semiconducting behavior. By using the seeded flux method, C. Li *et al.*⁴ succeeded to obtain large sized orthorhombic SiP crystals. They determined the optical bandgap as well as the charge carrier mobility, which was found to be ten times larger than that for MoS₂. Moreover, orthorhombic SiP crystals were found to be thermodynamically stable up to 1045°C. Finally, fast photoresponses suggested further that orthorhombic SiP crystals could be of interest for future optoelectronic applications. X. H. Li *et al.*¹⁹ investigated the crystallization of amorphous Si:P thin films prepared by co-evaporation of high purity Si and P. Depending on the P content, various crystallization products were identified in their films, including Si, orthorhombic SiP and a hexagonal Si₇P₃ phase which was later assigned to Si₁₂P₅²⁰. Very recently, based on DFT calculations, C. Li *et al.*²¹ identified the experimental Raman modes of orthorhombic SiP. Angle resolved polarized Raman spectroscopy was used to establish the anisotropy of the vibrational properties. In addition, photodetectors based on orthorhombic SiP were fabricated enabling highly sensitive detection

of polarized light. Finally, an attempt of SiP film growth by using a non-conventional chemical vapor deposition process was recently published²².

All previous works, which are mostly based on first principle calculations, show that 2D SiP is a promising material, which is expected to exhibit very appealing electronic and optoelectronic properties. However, till now, there is no report in the literature concerning the synthesis of monolayers of SiP. A possible route could be to start from SiP thin films but no report is still concerned with the growth of SiP thin films. In this paper, we investigate the growth of Si:P thin films by using co-evaporation of Si and P in ultra-high vacuum. In non-stoichiometric films, by using Raman spectroscopy supported by DFT calculations of the vibrational modes, we were able to identify orthorhombic SiP after annealing at temperatures larger than 950°C. Energy filtered transmission electron microscopy characterizations demonstrate the coexistence of both Si and SiP areas in the films with typical sizes of a few microns. Finally, high resolution scanning transmission electron microscopy (STEM) confirms the lamellar structure of the SiP grains while spatially resolved electron energy loss spectroscopy (EELS) measurements allows to obtain atomically resolved chemical maps of Si and P, which are in good agreement with the atomic model of orthorhombic SiP.

Experimental section

Experimental methods

The sample structure is the following: silicon substrate/SiO₂ (50 nm)/Si:P (40 at.% P, 200 nm)/SiO₂ (50 nm). Firstly, a 50 nm thick SiO₂ film was deposited using an e-beam gun on a Si(001) substrate held at room temperature. Secondly, a nominally 200 nm thick Si:P thin film was deposited by co-evaporation of Si from an e-beam gun and P vapor obtained from a GaP decomposition source²³. The Si flux was controlled by a quartz microbalance. The composition of the film was determined by X-ray photoelectron spectroscopy (XPS) using the Si 2*p* and P

$2p$ core levels. The obtained values were cross-checked by secondary ion mass spectroscopy (SIMS) measurements. We have considered in this study a sample containing 40 at. % of P, which corresponds to the maximum reproducible P content achievable with our GaP decomposition source. Thirdly, the Si:P film is capped by a 50 nm thick SiO₂ film. The role of the SiO₂ sandwiching films is to prevent P diffusion in the substrate and P desorption during annealing, i.e. to keep as much as possible the P atoms in the Si:P thin film. The samples were post-grown annealed at various temperatures ranging between 700°C and 1100°C in a rapid thermal annealing furnace for 5 minutes under nitrogen flow (200 sccm) at atmospheric pressure. Raman scattering measurements were performed at room temperature (RT) by using a 532 nm laser diode as excitation source operating at a power of 13 mW. The scattered light was analyzed by a monochromator equipped with a 1800 lines/mm grating and a charge coupled device (CCD) detector cooled at 200 K. The microstructural properties of the samples were investigated using energy-filtered transmission electron microscopy (EFTEM), scanning transmission electron microscopy (STEM), energy dispersive spectroscopy (EDS) and electron energy loss spectroscopy (EELS) using a JEOL ARM 200 F probe corrected with a cold field-emission gun equipped with a Gatan GIF Quantum energy filter. The microscope was operated at 80 KV. EDS and EELS spectrum images (SI) were recorded with a probe current of about 50 pA. Two EELS-SI were simultaneously recorded: one for the low-loss part containing the zero-loss, the other for the core loss, which allows advanced data post processing (correction of energy drift, multiple scattering corrections). The spectra were recorded with an electron beam having a half convergence angle of 24 mrad for a half collection angle of 56 mrad with an energy dispersion of 0.4 eV/channel and a pixel time of 0.005 s. A multivariate statistical analysis software (temDM MSA)²⁴ was used to improve the quality of the STEM-EELS data by de-noising the core-loss SI. Low-loss spectra were processed by zero-loss extraction and Fourier-log deconvolution for multiple scattering corrections. For TEM and STEM

observations, lamellas thinned up to $t/\lambda < 0.8$ (ratio between the thickness t and the electron mean free path λ) were prepared by focused ion beam (FIB) using a FEI Helios Nanolab 600i dual beam microscope. During FIB operation, the samples were capped by a pure carbon thin layer followed by a Pt-C layer to protect the sample during the first steps of the lamella extraction. After FIB milling, the lamellae were stored in vacuum to prevent oxidation.

Computational methods

Density functional theory (DFT) calculations were performed with the CRYSTAL17^{25,26} periodic computation code using the hybrid GGA-B3LYP functional^{25,26,27} complemented by an empirical dispersion correction term as proposed by Grimme²⁸ and a triple ζ localized (atom centered) basis set²⁹. This approach has been proven to model successfully vibrational features in periodic system with weak interactions such as molecular crystals³⁰. We adopted a periodic approach by considering an infinite crystal of SiP and SiP₂. The primitive cell is replicated in all directions according to the system symmetry. The reciprocal space was sampled according to a sublattice with the shrinking factor set to 8 (along the 3 lattice vectors), corresponding to respectively 105 and 260 independent k vectors in the irreducible part of the Brillouin zone for SiP and SiP₂. The DFT exchange–correlation contribution is evaluated by numerical integration through a (75 974) pruned grid (XLGRID keyword) over the unit cell volume. The atomic positions and the cell parameters were optimized for both SiP and SiP₂. The harmonic vibration frequencies were calculated at the Γ point and the corresponding intensities were evaluated through a coupled perturbed Kohn-Sham (CPKS) approach. The threshold on the self-consistent field energy was set to 10^{-8} Ha for the geometry optimization and 10^{-10} Ha for the frequency calculation.

Results and discussion

Figure 1 displays Raman spectra of both as grown and annealed Si:P thin films containing 40 at.% of P. The annealing temperature was varied between 700 and 1100°C. Several features can distinguished on the spectrum measured on the as-grown film. Apart from the Si-transverse optic (TO) line originating from the Si substrate at 520.5 cm^{-1} , one can identify several peaks at 475 cm^{-1} , 300 cm^{-1} and 170 cm^{-1} , which could correspond to the longitudinal optic (LO), longitudinal acoustic (LA) and transverse acoustic (TA) vibration modes of amorphous Si, respectively³¹. In addition, three other peaks are observed at 110 cm^{-1} , 233 cm^{-1} and 273 cm^{-1} , which could be related to the formation of an amorphous, metastable Si_xP_y compound. Annealing at temperatures up to 900°C leads to a decrease of the amorphous related peaks and to a concomitant increase of the Si-TO line indicating that crystallization of the thin film has started. Interestingly, for annealing temperatures larger than 950°C, the amorphous related features almost disappear while new and sharp features start to appear between 100 and 200 cm^{-1} , between 250 cm^{-1} and 300 cm^{-1} and close to 500 cm^{-1} . These peaks suggest the formation of crystalline phases. To identify the compound formed during annealing at temperatures larger than 950°C, we have considered the binary Si-P phase diagram³². Two stable compounds are generally identified which are SiP and SiP₂. In order to discriminate between both compounds, we have performed DFT calculations of the vibrational modes for SiP and SiP₂. Figure 2 shows the comparison between the experimental Raman spectrum measured after annealing a Si:P thin film containing 40 at.% of P at 1100°C and the calculated spectra for SiP (Fig. 2(a)) and SiP₂ (Fig. 2(b)). An excellent agreement is obtained between the experimental spectrum and the calculated one for SiP (Fig. 2(a)) if we exclude the peak at 520.5 cm^{-1} , which originates from the TO vibration of the crystalline Si substrate. The measured spectrum is further consistent with Raman measurements performed on orthorhombic SiP crystals prepared by the seeded flux growth method²¹. Meanwhile, we can observe a clear disagreement between the experimental spectrum and the calculated spectrum for SiP₂ (Fig.

2(b)). Table I summarizes the position of both measured and calculated vibrational wavenumbers for orthorhombic SiP and SiP₂ (to limit the number of lines, only the modes with an intensity > 0.5 % of the most intense peak have been reported). Some differences appear nevertheless between the experimental and theoretical values, which could be related either to the approximations used for the DFT calculations or, for the experimental spectrum, to deviations to the ideal crystal structure (strain effects or stacking faults). External modes at low wavenumbers (< 250 cm⁻¹) are particularly sensitive to this last effect. Grazing incidence X-ray diffraction measurements performed on a sample piece annealed at 1100°C further confirm the formation of SiP crystallizing in an orthorhombic structure (space group Cmc2₁, see Fig. S1 of the Supplementary Information). We can thus conclude that annealing at temperatures larger than 950°C leads to the formation of SiP in our thin films. In the following, we will investigate the microstructural properties of the Si:P thin films.

Figure 3(a) shows a high angle annular dark field (HAADF) STEM image of a cross section of the Si:P film containing 40 at. % of P. The interfaces appear vertically. The substrate is identified on the left side of the micrograph (zone 1) while the Si:P layer is sandwiched between two 50 nm thick SiO₂ layers. On the right side, a 15 nm thick carbon film is identified showing a dark contrast while the Pt-C capping layer shows a bright contrast. In the Si:P layer, two zones with a tiny contrast difference are visible in the HAADF image (identified as zone 3 and 4 in Fig. 3(a)). Since the heaviest elements diffuse more the electrons than the lightest, the contrast variation can be explained by a different chemical composition, the phosphorus content being higher in the brightest area (i.e. in zone 4). The EDS spectrum of zone 3 is dominated by a silicon related peak (Si_K, Fig. 3(b)). One can further identify two small peaks related to carbon (C_K) and phosphorus (P_K). The carbon related peak originates from contamination occurring during the measurement. A quantitative analysis yields a Si and P content of about 98 % and 2 %, respectively. In zone 4, the EDS spectrum shows both P_K and Si_K related peaks with the

same order of magnitude (Fig. 3(c)). The quantitative analysis yields a ratio between Si and P close to 1, which is compatible with SiP. The chemical analysis thus confirms that the observed contrast difference in the film can be linked to the presence of both SiP and P-doped Si phases. Nevertheless, since the areas appear very large (a few microns long), a Z contrast observation is not reliable enough to identify the phases because the thickness of the FIB lamella is never homogeneous on large areas. Plasmon imaging using either energy filtered transmission electron microscopy (EFTEM) or energy filtered scanning transmission electron microscopy (EFSTEM) is a well-established technique for investigating the Si-SiO₂ system for more than a decade^{33,34}. The EELS spectrum of pure silicon exhibits a sharp plasmon peak close to 17 eV while a broader peak centered near 24 eV is typical of SiO₂. To obtain an energy-filtered image, EELS is first used to collect an energy loss spectrum. Figure 3(d) reports processed EELS spectra extracted from a SI recorded on the central part of Fig 3(a). The substrate (zone 1) and the first SiO₂ layer (zone 2) show typical plasmon spectra of silicon and silica. The spectra recorded from zone 3 and from the SiP phase (zone 4) have a similar shape to that of the substrate. However, the spectrum taken from zone 4 is shifted towards 18.5 eV. The peak position difference between the silicon and the SiP related peaks allows EFTEM or EFSTEM imaging with a 2 eV large slit width as marked in figure 3(d). The images extracted from STEM-EELS SI centered at 16 eV, 19 eV and 25 eV are shown in figures 3(e), 3(f) and 3(g), respectively. The center of the energy window was shifted by 1 eV compared to the plasmon peaks in order to enhance the contrast between Si and SiP. As expected, the zone 3 is enlightened similarly to the substrate for an energy window centered at 16 eV (Fig 3(e)), while the SiO₂ layer appears in black and the SiP layer in light grey. When the energy window is centered at 19 eV, the SiP region is enlightened, while the Si zones appear grey (Fig. 3(f)). Finally, only SiO₂ is enlightened when the energy window is centered at 25 eV (Fig. 3(g)). Even if STEM-SI contains more information than EFTEM images, the STEM field of view is too

limited to image the large areas present in these samples, even at low magnification. Therefore, EFTEM was preferred to map the lamella. The EFTEM images shown in Figure 4 unveil large areas composed of either silicon phosphide or silicon. Both silicon and silicon phosphide areas are well separated. SiP precipitates in silicon (or the opposite) are never observed. In Fig. 4(b), silicon is only visible on the top of the micrograph while a more than 3 μm long SiP area is clearly visible. The presence of SiO_2 is further detected in the SiP area (Fig. 4(c)). This is due to the surface oxidation of the SiP area that occurs during the handling of the lamella in air. One can note that for a 50 nm thick lamella already observed by TEM, SiP appears fully oxidized after a few days of air exposure. The rapid oxidation in air is probably favored by the surface amorphization caused by the preparation of the lamella and by the electron irradiation damages during the first observation. Moreover, STEM-ADF imaging reveals that the large SiP areas are not single crystalline (in STEM-ADF imaging the contrast in the image is related to the grain orientation). The structure of SiP was determined by analysing electron diffraction patterns and fast Fourier transform (FFT) patterns of HRSTEM images showing grains with various orientations. The SiP phase was identified as orthorhombic structure (space group $\text{Cmc}2_1$), in good agreement with grazing incidence X-ray diffraction measurements. Figure 5(a) shows a HRSTEM-HAADF image of a SiP grain oriented along the $[100]$ zone axis. The inset shows a coloured FFT of the micrograph. In this image the a -axis is set perpendicular to the image while the b -axis is horizontal and the c -axis is vertical. One can clearly see the lamellar structure perpendicularly to the c -axis. Figure 5(f) shows the atomic structure with the same orientation (the P atoms are indicated in green and the Si atoms in red). The structure can be described as a stack of A-type and B-type layers of silicon sandwiched between two P planes. The alternation of A- and B-type layers is clearly visible in the HRSTEM image shown Fig. 5(a), by paying attention on the orientation of the basic building blocks of each layer. Stacking faults were commonly seen in high resolution images. In this case, the building blocks of neighbouring

layers have the same orientation. It results in a lack of alternating A- and B-type layers, as it can be seen on the top of the red rectangle drawn in Figure 5(a). They can be also seen in the STEM-HAADF image for the [310] zone axis direction (see Fig. S2 in the Supplementary Information). To support our observations, a high spatial resolution STEM-EELS SI was recorded in the rectangular area drawn in Figure 5(a), with a sampling of 0.03 nm. Figure 5(b) shows the EELS spectrum obtained by integrating all the spectra recorded in the SI after energy-drift correction, de-noising, background subtraction and multiple scattering corrections. $\text{Si}_{\text{L}1}$, $\text{Si}_{\text{L}3}$, $\text{P}_{\text{L}3}$ and $\text{P}_{\text{L}1}$ edges positions are pointed out on the spectrum. The signals of Si_{L} and P_{L} are overlapping. To get a chemical map, it is necessary to extract individual signals from the spectra. We have performed a least square fitting of each spectrum contained in the SI by using reference spectra as described in a previous paper³⁵. The reference spectrum of Si was measured on a Si substrate and that of P was extracted from data recorded on orthorhombic SiP_2 ³⁵. The reference spectra were collected with the same experimental conditions than that of the present work (sample thickness, convergence and collection angle, spectrometer dispersion) and were processed with the same basic procedure (energy-drift correction, principal component analysis (PCA) de-noising, multiple scattering correction). The elemental maps were drawn from the results of the fit. Figure 5(c) and 5(d) show quantitative chemical maps drawn for Si and for P, respectively. The noise in the images was partly removed by applying a radial Wiener filter to improve the quality of the maps. Figure 5(e) was obtained by the superposition of the Si- and P-related maps shown in Figs. 5(c) and (d). The final resolution obtained for the chemical map is sufficient to clearly identify the atomic positions of both Si and P and the orientation of the building blocks in the different layers. The chemical map shown in Fig. 5(e) and the atomic model drawn with the same magnification (Fig. 5(f)) can be perfectly superimposed, except for the first and the second layer of the chemical map where the building blocks have the same orientation due to a stacking fault.

Conclusions

To summarize, we have studied the structural and the vibrational properties of Si:P thin films obtained by using co-evaporation of both Si and P in ultra-high vacuum. We have shown that annealing at temperatures higher than 950°C leads to the formation of crystalline phases. DFT calculations of the vibrational modes allowed us to identify orthorhombic SiP. Low loss EELS allowed us to identify a plasmon resonance for SiP at 18.5 eV. This allows imaging the phase distribution in the film by EFTEM. Detailed STEM and EF(S)TEM investigations showed large polycrystalline SiP areas (a few micron large). The SiP areas are found to coexist with large areas of Si grains containing around 2 at.% of P in the films. STEM-HAADF imaging along the [100] zone axis direction gave evidence of the lamellar structure of the SiP grains. Finally, EDS measurements and atomically-resolved EELS chemical maps further confirmed the stoichiometry and structure of SiP. Our work represents an important step towards the synthesis and characterization of 2D-SiP, which is expected to exhibit exciting electronic and optoelectronic properties.

Supporting Information

Grazing incidence X-ray diffraction patterns for Si:P thin films with different P contents after annealing at 1100°C for 5 minutes; STEM-HAADF image of a SiP grain oriented along the [310] zone axis with its corresponding Fourier transform and the atomic structure giving evidence of stacking faults in the grain.

Acknowledgments

The authors would like to acknowledge the French PIA project “Lorraine Université d’Excellence”, reference No. ANR-15IDEX-04-LUE and the ANR project DONNA (ANR-18-CE09-0034) for support. High performance computing resources were partially provided by the EXPLOR center hosted by Université de Lorraine.

*corresponding author: mathieu.stoffel@univ-lorraine.fr

Figure captions

Figure 1: Raman spectra measured at room temperature for Si:P thin films containing 40 at.% of P prior to and after annealing at various temperatures ranging between 700°C and 1100°C.

Figure 2: Comparison between the Raman spectrum measured after annealing a Si:P thin film containing 40 at. % at 1100°C (green solid line) and the calculated spectrum for SiP (a) and SiP₂ (b) (magenta solid lines).

Table I: Measured (ω_{exp}) and calculated (ω_{DFT}) vibrational wavenumbers of orthorhombic SiP and SiP₂. The symmetry species of the vibrational modes are indicated in parentheses.

Figure 3: a) STEM-HAADF micrograph showing a cross section of the Si:P thin film containing 40 at.% of P. The interfaces between the layers are set vertically. The Si substrate is identified on the left (area 1). The black layer on the right followed by a strong white contrast shows respectively C and Pt-C layers deposited during the FIB procedure, b) EDS spectrum recorded on area 3, c) EDS spectrum recorded on area 4, d) Deconvoluted EELS spectra recorded respectively on areas 1, 2, 3 and 4. A 2 eV large window is drawn on the figure, e), f), g) EFSTEM images extracted from SI with an energy window of 2 eV width, respectively centered at e) 16 eV to image Si, f) 19 eV to image SiP, g) 25 eV to image SiO₂.

Figure 4: Low magnification EFTEM image recorded with a slit width of 2 eV showing large Si and SiP areas. a) Slit centered at 16 eV for location of Si, b) Slit centered at 19 eV for location of SiP, c) Slit centered at 25 eV for location of SiO₂

Figure 5: a) High-resolution STEM-HAADF image of a SiP crystal. The inset shows a FFT with the [100] orientation, b) Background subtracted, and multiple scattering corrected EELS spectrum extracted from EELS-SI recorded in the area delimited by a red solid line in (a). c), d) Quantitative chemical maps with atomic resolution for Si (in red) and P (in green) drawn by processing EELS-SI, e) Superposition of P and Si maps, f) Structural model of SiP for the [100] orientation with Si atoms in red and P atoms in green.

References

- (1) Beck C. G.; Stickler R. Crystallography of SiP and SiAs single crystals and of SiP precipitates in Si. *J. Appl. Phys.* **1966**, *37*, 4683-4687.
- (2) Wadsten T. Crystal structures of SiP₂, SiAs₂ and GeP. *Acta Chimica Scandinavica* **1967**, *21*, 593-594.
- (3) Barreteau C.; Michon B.; Besnard C.; Giannini E. High pressure melt growth and transport properties of SiP, SiAs, GeP and GeAs 2D layered semiconductors. *Journal of Crystal Growth* **2016**, *443*, 75-80.
- (4) Li C.; Wang S.; Zhang X.; Jia N.; Yu T.; Zhu M.; Liu D.; Tao X. Controllable seeded flux growth and optoelectronic properties of bulk o-SiP crystals. *Cryst. Eng. Comm.* **2017**, *19*, 6986-6991.
- (5) Zhang S.; Guo S.; Chen Z.; Wang Y.; Gao H.; Gómez-Herrero J.; Ares P.; Zamora F.; Zhu Z.; Zeng H. Recent progress in 2D group VA semiconductors: from theory to experiment. *Chem. Soc. Rev.* **2018**, *47*, 982-1021
- (6) Guo S.; Zhang Y.; Ge Y.; Zhang S.; Zeng H.; Zhang H. 2D V-V binary materials: status and challenges. *Adv. Mat.* **2019**, *31*, 1902352
- (7) Ashton M.; Sinnott S. B.; Hennig R. G. Computational discovery and characterization of polymorphic two-dimensional IV-V materials. *Appl. Phys. Lett.* **2016**, *109*, 192103.
- (8) Shu H. Electronic, transport and optical properties of atomically thin silicon phosphide: first-principles calculations. *Mat. Res. Express* **2019**, *6*, 026428.
- (9) Zhang S.; Guo S.; Huang Y.; Zhu Z.; Cai B.; Xie M.; Zhou W.; Zeng H. Two-dimensional SiP: an unexplored direct band-gap semiconductor. *2D Materials* **2017**, *4*, 015030.
- (10) Özdamar B.; Özbal G.; Neşet Çinar M.; Sevim K.; Kurt G.; Kaya B.; Sevinçli H. Structural, vibrational and electronic properties of single-layer hexagonal crystals of group IV and V elements. *Phys. Rev. B* **2018**, *98*, 045431.

- (11) Malyi O. I.; Sopiha K. V.; Radchenko I.; Wu P.; Persson C. Tailoring electronic properties of multilayer phosphorene by siliconization. *Phys. Chem. Chem. Phys.* **2018**, *20*, 2075-2083.
- (12) Huang B.; Zhuang H. L.; Yoon M.; Sumpter B. G.; Wei S. H. Highly stable two-dimensional silicon phosphides: different stoichiometries and exotic electronic properties. *Phys. Rev. B*, **2015**, *91*, 125401 (R).
- (13) Mortazavi B.; Rabczuk T. Anisotropic mechanical properties and strain-tunable bandgap in single layer SiP, SiAs, GeP and GeAs. *Physica E* **2018**, *103*, 273-278.
- (14) Kansara S.; Dev Bhuyan P.; Sonvane Y.; Gupta S. K. Two-dimensional silicon phosphide: low effective mass and direct band gap for future devices applications. *J. Mater. Sci.* **2019**, *54*, 11878-11888.
- (15) Ma Z.; Zhuang J.; Zhang X.; Zhou Z. SiP monolayers: new 2D structures of group IV-V compounds for visible light photohydrolytic catalysts. *Front. Phys.* **2018**, *13*, 138104.
- (16) Mortazavi B.; Shahrokhi M.; Cuniberti G.; Zhuang X. Two-dimensional SiP, SiAs, GeP and GeAs as promising candidates for photocatalytic applications. *Coatings* **2019**, *9*, 522.
- (17) Jiang E.; Zhu X.; Ouyang T.; Tang C.; Li J.; He C.; Zhang C.; Zhong J. The thermoelectric properties of monolayer SiP and GeP from first-principles calculations. *J. Appl. Phys.* **2019**, *126*, 185106.
- (18) Zhu Y.; Wang X.; Mi W. Strain and electric field modulated electronic structure of two-dimensional SiP(SiAs)/GeS van der Waals heterostructures. *J. Mat. Chem. C* **2019**, *7*, 10491-10497.
- (19) Li X. H.; Carlsson J. R. A.; Gong S. F.; Hentzell H. T. G. Thermal stability and crystallization products of amorphous Si:P alloy thin films made by coevaporation of Si and P. *J. Appl. Phys.* **1994**, *76*, 5179-5184.

- (20) Carlsson J. R. A.; Madsen L. D.; Johansson M. P.; Hultman L.; Li X. H.; Hentzell H. T. G.; Wallenberg L. R. A new silicon phosphide, Si₁₂P₅: formation conditions, structure and properties. *J. Vac. Sci. Technol. A* **1997**, *15*, 394-401.
- (21) Li C.; Wang S.; Li C.; Yu T.; Jia N.; Qiao J.; Zhu M.; Liu D.; Tao X. Highly sensitive detection of polarized light using a new group IV-V 2D orthorhombic SiP. *J. Mat. Chem. C* **2018**, *6*, 7219-7225.
- (22) Wen Z.; Wang Y.; Chen Z.; Shi J. Chemical vapor growth of silicon phosphide nanostructures. *MRS advances* **2020**, *5*, 1653-1660.
- (23) Lippert G.; Osten H. J.; Krüger D.; Gaworzewski P.; Eberl K. Heavy phosphorus doping in molecular beam epitaxial grown silicon with a GaP decomposition source. *Appl. Phys. Lett.* **1995**, *66*, 3197-3199.
- (24) Potapov P. Why principal component analysis of STEM spectrum-images results in “abstract”, uninterpretable loadings? *Ultramicroscopy*, **2016**, *160*, 197-212.
- (25) Dovesi R.; Erba A.; Orlando R.; Zicovich-Wilson C. M.; Civalieri B.; Maschio L.; Rérat M.; Casassa S.; Baima J.; Salustro S.; Kirtman B. Quantum-mechanical condensed matter simulations with CRYSTAL. *WIREs-Comput. Mol. Sci.* **2018**, *8*, e1360
- (26) Dovesi R.; Saunders V. R.; Roetti C.; Orlando R.; Zicovich-Wilson C. M.; Pascale F.; Maschio L.; Erba A.; Rérat M.; Casassa S. *CRYSTAL17 User's Manual*, **2017**, University of Torino, Torino.
- (27) Becke A. D. Density functional thermochemistry III: The role of exact exchange. *J. Chem. Phys.* **1993**, *98*, 5648-5652.
- (28) Grimme S. Semi-empirical GGA type density functional constructed with a long range dispersion correction. *J. Comput. Chem.* **2006**, *27*, 1787-1799.

- (29) Vilela Oliveira D.; Laun J.; Peintinger M. F.; Bredow T. BSSE correction scheme for consistent Gaussian basis sets of double-and triple-zeta valence with polarization quality for solid state calculations. *J. Comput. Chem.* **2019**, *40*, 2364-2376.
- (30) Civalleri B.; Zicovich-Wilson C. M.; Valenzano L.; Ugliengo P. B3LYP augmented with an empirical dispersion term (B3LYP-D*) as applied to molecular crystals. *Cryst. Eng. Comm.* **2008**, *10*, 405-410.
- (31) Marinov M.; Zotov N. Model investigation of the Raman spectra of amorphous silicon. *Phys. Rev. B* **1997**, *55*, 2938-2944.
- (32) Liang S. M.; Schmid-Fetzer R. Modelling of thermodynamic properties and phase equilibria of the Si-P system. *Journal of Phase Equilibria and Diffusion* **2014**, *35*, 24-35.
- (33) Nicotra G.; Lombardo S.; Spinella C.; Ammendola G.; Gerardi C.; Demuro C. Observation of the nucleation kinetic of Si quantum dots on SiO₂ by energy filtered transmission electron microscopy. *Appl. Surf. Sci.* **2003**, *205*, 304-308.
- (34) Schamm S.; Bonafos C.; Coffin H.; Cherkashin N.; Carrada M.; Ben Assayag G.; Claverie A.; Tence M.; Colliex C. Imaging Si nanoparticles embedded in SiO₂ layers by (S)TEM-EELS. *Ultramicroscopy* **2008**, *108*, 346–357.
- (35) Geiskopf S.; Stoffel M.; Devaux X.; André E.; Carteret C.; Bouché A.; Vergnat M.; Rinnert H. Formation of SiP₂ nanocrystals embedded in SiO₂ from phosphorus-rich SiO_{1.5} thin films. *J. Phys. Chem. C* **2020**, *124*, 7973-7978.

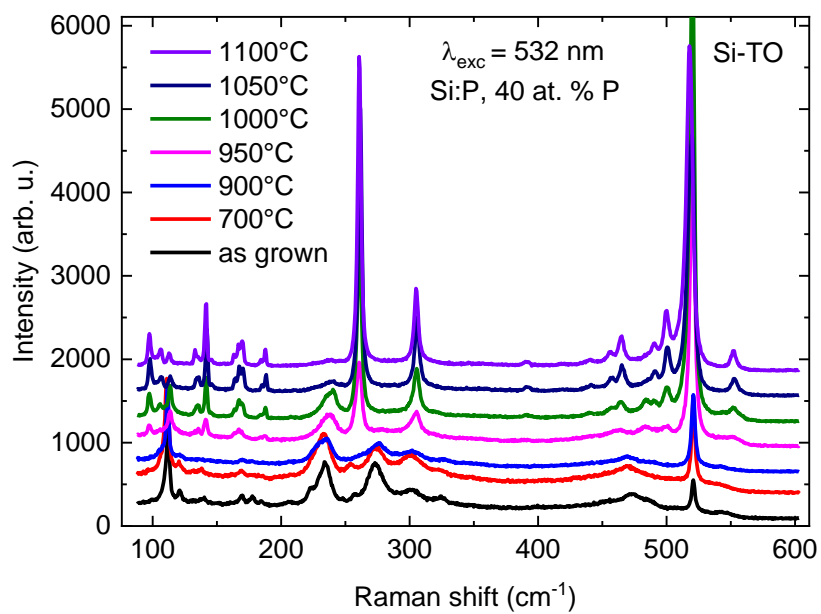


Fig.1

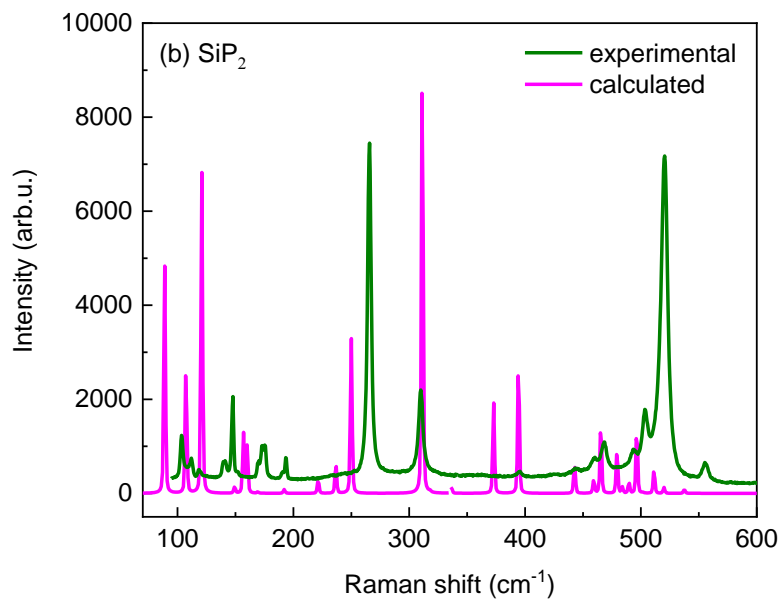
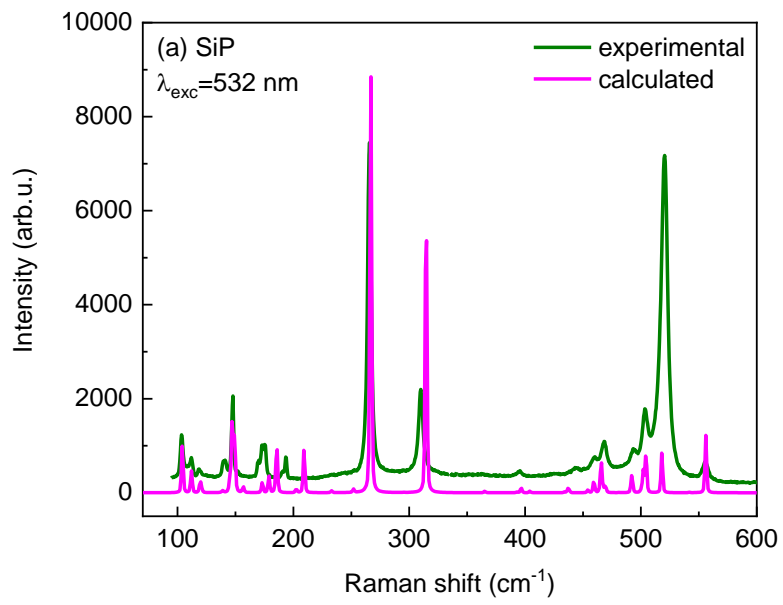


Fig.2

$\omega_{\text{EXP}} (\text{cm}^{-1})$	$\omega_{\text{DFT}} \text{ for SiP} (\text{cm}^{-1})$	$\omega_{\text{DFT}} \text{ for SiP}_2 (\text{cm}^{-1})$
	36 (A2)	32 (B3g)
	49 (A1)	37 (Ag)
104	104 (B1)	89 (Ag)
112	112 (A1)	107 (B1g)
119	119 (B2)	108 (B2g)
	120 (A2)	121 (Ag)
141	145 (A2)	
147	147 (B2)	
151	149 (B1)	149 (B1g)
	157 (B2)	157 (B3g)
170	173 (A1)	160 (B2g)
173	179 (B2)	
175	186 (B1)	192 (B3g)
191	202 (A1)	221 (B1g)
193	209 (B1)	237 (Ag)
	252 (A1)	250 (Ag)
266	267 (A1)	251 (B1g)
310	315 (A1)	311 (Ag)
		336 (B1g)
		373 (Ag)
396	397 (A1)	394 (B2g)
		394 (B3g)
444	437 (B2)	442 (B1g)
460	454 (A2)	443 (Ag)
	459 (B1)	459 (B1g)
	460 (A1)	
	465 (A2)	465 (Ag)
468	466 (B2)	
	469 (B2)	
	470 (A2)	479 (Ag)
		484 (B2g)
493	492 (A1)	490 (B3g)
	493 (B1)	496 (Ag)
503	502 (A1)	
	504 (B1)	511 (B1g)
520.5*, (511.5)	518 (A1)	520 (Ag)
555	556 (A1)	537 (B1g)

*Si stretching mode of the silicon wafer (a band belonging to the SiP compound has been fitted at 511.5 cm^{-1})

Table I

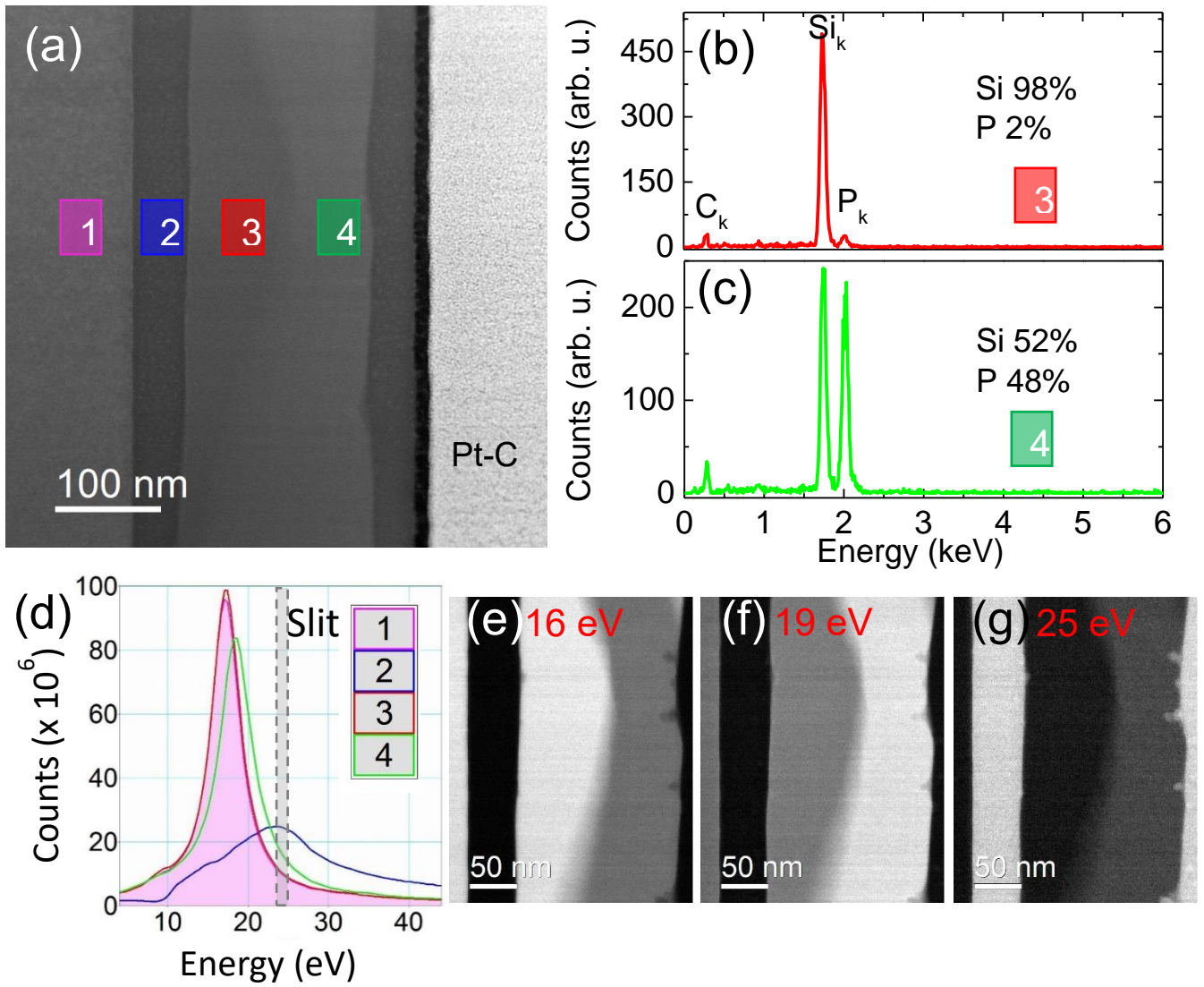


Fig. 3

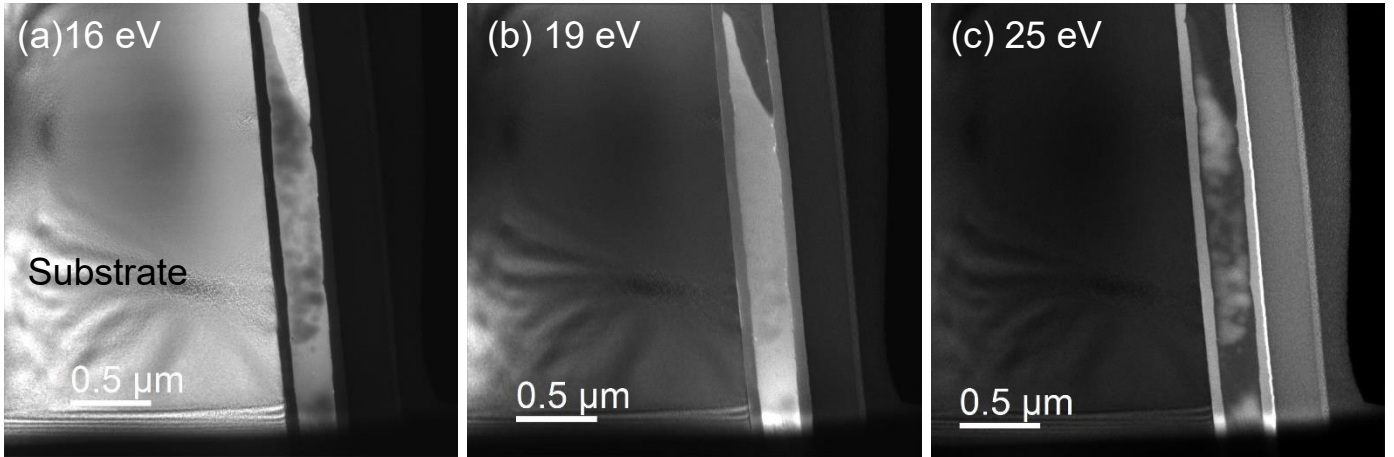


Fig. 4

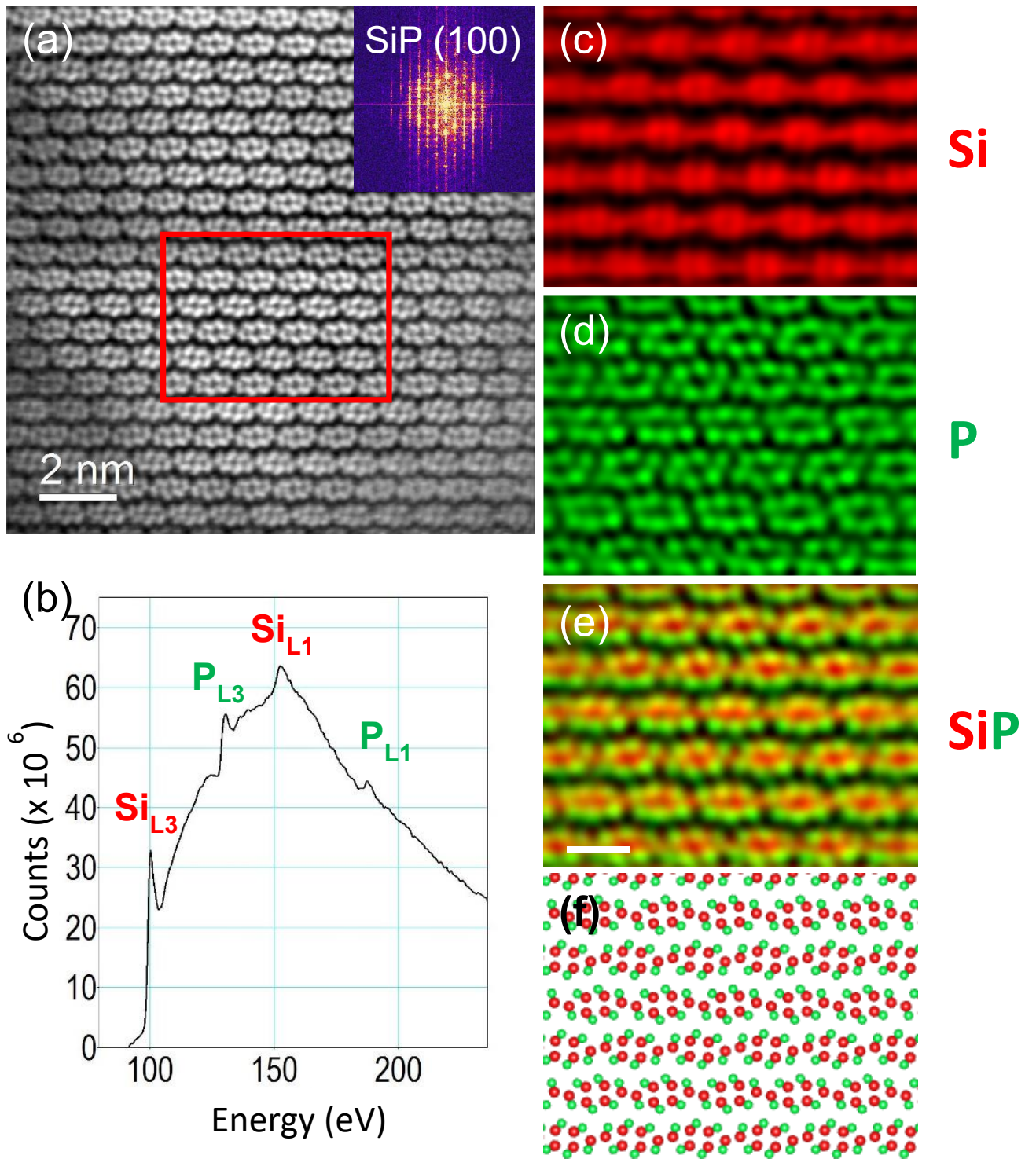
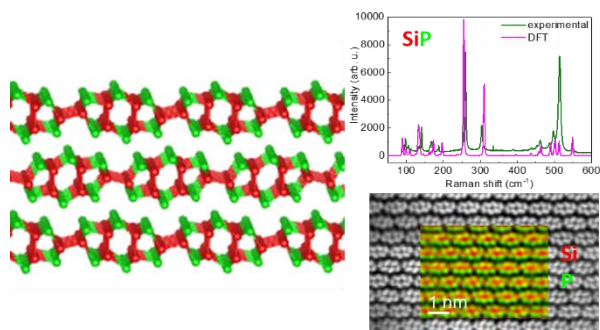


Fig. 5



TOC graphic